



HIP 33609 b: An Eccentric Brown Dwarf Transiting a $V = 7.3$ Rapidly Rotating B Star

Noah Vowell¹, Joseph E. Rodriguez¹, Samuel N. Quinn², George Zhou³, Andrew Vanderburg⁴, Andrew W. Mann⁵, Matthew J. Hooton⁶, Keivan G. Stassun^{7,8}, Saburo Howard⁹, Allyson Bieryla², David W. Latham², Steve B. Howell¹⁰, Tristan Guillot⁹, Carl Ziegler¹¹, Karen A. Collins², Theron W. Carmichael¹², Jon M. Jenkins¹⁰, Avi Shporer⁴, Lyu ABE⁹, Philippe Bendjoya⁹, Jonathan L. Bush⁵, Marco Buttu¹³, Kevin I. Collins¹⁴, Jason D. Eastman², Matthew J. Fields⁵, Thomas Gasparotto¹⁵, Maximilian N. Günther¹⁶, Veselin B. Kostov^{17,18}, Adam L. Kraus¹⁹, Kathryn V. Lester¹⁰, Alan M. Levine⁴, Colin Littlefield^{10,20}, Wenceslas Marie-Sainte²¹, Djamel Mékarnia⁹, Hugh P. Osborn^{4,22}, David Rapetti^{10,23}, George R. Ricker⁴, S. Seager^{4,24,25}, Ramotholo Sefako²⁶, Gregor Srdoc²⁷, Olga Suarez⁹, Guillermo Torres², Amaury H. M. J. Triard²⁸, R. Vanderspek⁴, and Joshua N. Winn²⁹

¹Center for Data Intensive and Time Domain Astronomy, Department of Physics and Astronomy, Michigan State University, East Lansing, MI 48824, USA; vowellno@msu.edu

²Center for Astrophysics | Harvard & Smithsonian, 60 Garden Street, Cambridge, MA 02138, USA

³University of Southern Queensland, West Street, Darling Heights QLD 4350, Australia

⁴Department of Physics and Kavli Institute for Astrophysics and Space Research, Massachusetts Institute of Technology, Cambridge, MA 02139, USA

⁵Department of Physics and Astronomy, The University of North Carolina at Chapel Hill, Chapel Hill, NC 27599, USA

⁶Cavendish Laboratory, JJ Thomson Avenue, Cambridge, CB3 0HE, UK

⁷Department of Physics and Astronomy, Vanderbilt University, Nashville, TN 37235, USA

⁸Department of Physics, Fisk University, 1000 17th Avenue North, Nashville, TN 37208, USA

⁹Université Côte d'Azur, Observatoire de la Côte d'Azur, CNRS, Lagrange Laboratory, Nice, France

¹⁰NASA Ames Research Center, Moffett Field, CA 94035, USA

¹¹Department of Physics, Engineering and Astronomy, Stephen F. Austin State University, 1936 North Street, Nacogdoches, TX 75962, USA

¹²Institute for Astronomy, University of Edinburgh, Royal Observatory, Blackford Hill, Edinburgh, EH9 3HJ, UK

¹³INAF—Osservatorio Astronomico di Cagliari, Cagliari, Italy

¹⁴George Mason University, 4400 University Drive, Fairfax, VA 22030 USA

¹⁵Institute of Polar Sciences—CNR, via Torino, 155 I-30172 Venice-Mestre, Italy

¹⁶European Space Agency (ESA), European Space Research and Technology Centre (ESTEC), Keplerlaan 1, 2201 AZ Noordwijk, The Netherlands

¹⁷NASA Goddard Space Flight Center, 8800 Greenbelt Road, Greenbelt, MD 20771, USA

¹⁸SETI Institute, 189 Bernardo Ave, Suite 200, Mountain View, CA 94043, USA

¹⁹Department of Astronomy, The University of Texas at Austin, Austin, TX 78712, USA

²⁰Bay Area Environmental Research Institute, Moffett Field, CA 94035, USA

²¹Institut Paul Emile Victor, Concordia Station, Antarctica

²²Physikalisches Institut, University of Bern, Gesellschaftstrasse 6, 3012 Bern, Switzerland

²³Research Institute for Advanced Computer Science, Universities Space Research Association, Washington, DC 20024, USA

²⁴Department of Earth, Atmospheric, and Planetary Sciences, Massachusetts Institute of Technology, Cambridge, MA 02139, USA

²⁵Department of Aeronautics and Astronautics, Massachusetts Institute of Technology, Cambridge, MA 02139, USA

²⁶South African Astronomical Observatory, P.O. Box 9, Observatory 7935, Cape Town, South Africa

²⁷Kotizarovci Observatory, Sarsoni 90, 51216 Viskovo, Croatia

²⁸School of Physics & Astronomy, University of Birmingham, Edgbaston, Birmingham B15 2TT, UK

²⁹Department of Astrophysical Sciences, Princeton University, Princeton, NJ 08544, USA

Received 2023 January 24; revised 2023 April 26; accepted 2023 April 26; published 2023 June 5

Abstract

We present the discovery and characterization of HIP 33609 b, a transiting warm brown dwarf orbiting a late B star, discovered by NASA's Transiting Exoplanet Survey Satellite as TOI-588 b. HIP 33609 b is a large ($R_b = 1.580^{+0.074}_{-0.070} R_J$) brown dwarf on a highly eccentric ($e = 0.560^{+0.029}_{-0.031}$) orbit with a 39 days period. The host star is a bright ($V = 7.3$ mag), $T_{\text{eff}} = 10,400^{+800}_{-660}$ K star with a mass of $M_* = 2.383^{+0.10}_{-0.095} M_\odot$ and radius of $R_* = 1.863^{+0.087}_{-0.082} R_\odot$, making it the hottest transiting brown dwarf host star discovered to date. We obtained radial velocity measurements from the CHIRON spectrograph confirming the companion's mass of $M_b = 68.0^{+7.4}_{-7.1} M_J$ as well as the host star's rotation rate ($v \sin i_* = 55.6 \pm 1.8 \text{ km s}^{-1}$). We also present the discovery of a new comoving group of stars, designated as MELANGE-6, and determine that HIP 33609 is a member. We use a combination of rotation periods and isochrone models fit to the cluster members to estimate an age of 150 ± 25 Myr. With a measured mass, radius, and age, HIP 33609 b becomes a benchmark for substellar evolutionary models.

Unified Astronomy Thesaurus concepts: Exoplanets (498); Brown dwarfs (185); Young star clusters (1833); Direct imaging (387); CCD photometry (208); High resolution spectroscopy (2096); Exoplanet evolution (491)

Supporting material: data behind figure

1. Introduction

Brown dwarfs (BDs), defined as objects that fuse only deuterium at some point in their lifetime, occupy the region in mass between planets and stars. The mass range corresponding to this historical definition runs between a lower limit of 11–16

Jupiter Masses (M_J), where an object begins to fuse deuterium (Spiegel et al. 2011) and an upper limit of 75–80 MJ where hydrogen fusion begins (Baraffe et al. 2002). However, these fusion based transitions that distinguish BDs from planets and stars may occur at masses that depend on multiple factors. Specifically, the environment that the object formed in, the effects of convection on the object, and its metallicity can influence these traditional mass limits (Spiegel et al. 2011). Therefore, it may be preferable to define BDs in the context of their formation and evolution, an idea suggested by Chabrier et al. (2014), Burrows et al. (2001), and Carmichael et al. (2021).

It is likely that some BDs form and evolve in similar ways to giant planets, providing the opportunity for comparative studies with the known exoplanet sample and possibly gaining insight into the evolutionary pathways of BDs. We know that planets can migrate through quiet mechanisms like disk-driven migration (D’Angelo et al. 2003) as well as dynamical interactions such as planet–planet scattering or Kozai–Lidov cycles (Kozai 1962; Lidov 1962; Fabrycky & Tremaine 2007). Such dynamical interactions lead to a fraction of the population residing in close-in, highly misaligned as well as highly eccentric orbits (Rasio & Ford 1996; Wu & Lithwick 2011). We can measure these misalignments using Doppler tomography (Collier Cameron et al. 2010; Zhou et al. 2016) and the Rossiter–McLaughlin effect. These techniques constrain the orbital obliquity of the companion by tracking the effects of the transiting planet’s shadow on the rotationally broadened stellar spectral line profile or on the apparent radial velocity of the host star. If BDs are indeed subject to the same dynamical interactions as planets, then we should expect to see similar signatures in the transiting BD population.

In order to fully understand the formation and evolutionary history of BDs, we need robust, well-tested models for substellar evolution. Current substellar evolutionary models show that BDs rapidly contract in the first billion years after formation (Burrows et al. 2001; Baraffe et al. 2003; Saumon & Marley 2008; Phillips et al. 2020), and then continue slowly contracting out to ~ 10 Gyr. Combining this with the fact that BDs are held up by electron degeneracy pressure and therefore, at late times, tend to have radii that decrease with mass reveals the significance of obtaining precise age estimates for transiting BDs. Thus, in order to test our models of substellar evolution, we need precise, independent measurements of BD radii, masses, and ages. Through the combined efforts of NASA’s Transiting Exoplanet Survey Satellite (TESS; Ricker et al. 2015), ground-based follow-up programs, and ESA’s Gaia mission (Gaia Collaboration et al. 2022) we are able to obtain precise measurements of transiting BD radii and masses with transit photometry, radial velocity measurements, spectral energy distributions (SEDs), and Gaia parallaxes.

Precisely measuring the age of the BD, while difficult, is vital to furthering our understanding of BD evolution because it provides a direct test of substellar evolutionary models. Unfortunately, only four of the 37 published transiting BD systems have precisely measured ages ($>3\sigma$) determined either through stellar cluster memberships (Gillen et al. 2017; Beatty et al. 2018; David et al. 2019) or leveraging gyrochronology and lithium abundances (Carmichael et al. 2021). The simplest method for obtaining precise ages of BDs would be to discover more around host stars that are members of clusters. This kind of targeted discovery is already underway for planets by the

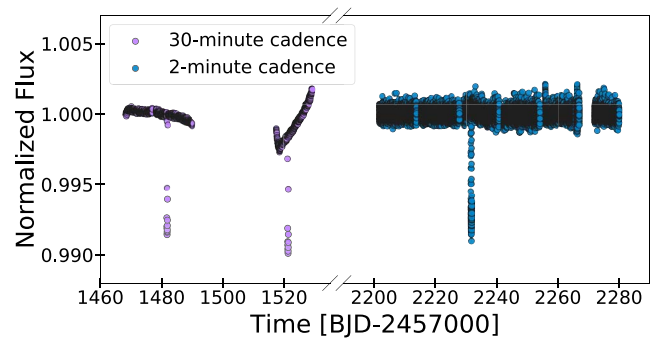


Figure 1. The TESS light curves from sectors 6, 8, 33, 34, and 35 extracted using the techniques described in Section 2.1. We note that the gap in flux located at BJD 2459270 is caused by a period of coarse pointing. These poor data were removed in our fit as described in Section 2.1.

TESS Hunt for Young and Maturing Exoplanets consortium (Newton et al. 2019) and can also be applied to BDs in order to better understand their evolutionary pathways.

In this paper, we present the discovery of HIP 33609 b from NASA’s TESS mission. HIP 33609 b adds to the growing number of transiting BDs discovered by TESS that is approaching a population large enough to begin performing robust demographic analyses. It is also a benchmark system for testing BD formation and evolution since it has an age measurement from membership in a stellar association, and its host star is both the brightest ($V=7.3$ mag) and hottest ($T_{\text{eff}}=10,400^{+800}_{-660}$ K) star with a transiting BD companion discovered so far. HIP 33609 b’s high orbital eccentricity ($e=0.560^{+0.029}_{-0.031}$) could be indicative of a dynamically active past, and we should therefore search for additional evidence of past interactions (such as a large stellar obliquity). In Section 2 we present our follow-up photometric and spectroscopic observations obtained through the TESS Follow-up Observing Program (TFOP) Working Group. We establish HIP 33609’s cluster membership and age in Section 3. In Section 4 we describe our global modeling methodology using EXOFASTv2 (Eastman et al. 2013, 2019) as well a separate analysis on the effects of gravity darkening. We place HIP 33609 b in context with other transiting substellar companions and discuss future characterization prospects in Section 5. We present our conclusions in Section 6.

2. Observations

To measure the mass and orbital parameters of the HIP 33609 system, we used a combination of photometric (Figures 1 and 2) and spectroscopic (Figure 3) observations. The observations, gathered through TFOP, were part of the vetting process to rule out false-positive scenarios. We describe these observations in the following subsections.

2.1. TESS Photometry

TESS observes a $24^\circ \times 96^\circ$ patch of the sky for approximately 27 days before moving to a new sector (Ricker et al. 2015). In the prime mission, it observed its entire field of view at 30 minutes cadence, and a preselected set of stars were observed at 2 minutes cadence, resulting in $>80\%$ of the entire sky being observed. TESS just completed its first extended mission in which it observed a portion of the ecliptic plane, the region of sky observed by the *K2* mission (Howell et al. 2014), which repurposed the Kepler spacecraft to observe the ecliptic

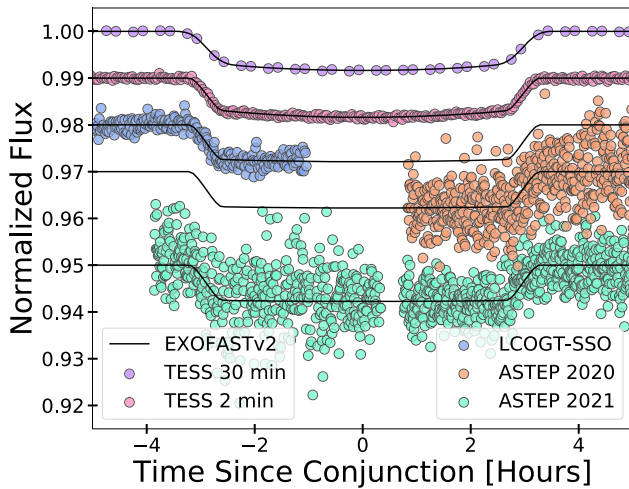


Figure 2. The TESS and ground-based follow-up transits for HIP 33609 b described in sections Sections 2.1 and 2.2. The model for each transit is shown as a black solid line.

plane after the loss of the spacecraft’s second of four reaction wheels. This region was not observed during the TESS prime mission, but a portion was observed over a 5 month period in the first extended mission, and another portion will be observed over a 4 month period in the second extended mission which started 2022 September 2. A subset of ~ 2000 of the 20,000 preselected targets in the extended missions³⁰ are observed at 20 s cadence in addition to 2 minutes cadence, and the exposure time for the full-frame images (FFI) was reduced to 10 minutes in the first extended mission, and further reduced to just 200 seconds in the second extended mission. HIP 33609 b was first observed during the primary mission in the sector six FFIs at 30 minutes cadence in 2018 and then again in sector 8 in 2019. TESS then observed HIP 33609 again during its first extended mission at 2 minutes cadence in 2021 during sectors 33, 34, and 35.

TESS observations are downloaded, reduced, and analyzed on the ground. The original detection of a transiting signal around HIP 33609 was made by the MIT Quick-Look Pipeline, and it was then vetted as a TESS Object of Interest (TOI-588, Table 1) using the process described by Guerrero et al. (2021). In subsequent observations, the data collected by TESS at 2 minutes cadence were processed by the Science Processing Operations Center (SPOC) pipeline (Jenkins et al. 2016) based at NASA Ames Research Center where the image data were calibrated, and light curves were extracted for each target, which were then searched for transiting planet signatures. We then downloaded these SPOC PDC-SAP light curves (Smith et al. 2012; Stumpe et al. 2012, 2014) from the Mikulski Archive for Space Telescopes using the *Lightkurve 2* software (Lightkurve Collaboration et al. 2018). The SPOC transit search over sectors 34 and 35 triggered on the single transit of HIP 33609 b in sector 34, but at the wrong period. Nevertheless, the difference image centroiding test located the source of the transit signature within $1''.2 \pm 2''.8$. We conducted a Lomb–Scargle period search on the 2 minutes, normalized light curve with the transits masked out to search for stellar rotation from star spots. We searched for periods ranging from 0.1 to 10 days and found no significant signal as expected from a relatively quiet B-type star.

We found a total of four transits of HIP 33609 in sectors 6, 8, 34, and 35. However, we discarded the sector 35 transit due to poor data quality caused by a period of unstable pointing of the TESS spacecraft. During this period, the stars moved around significantly on the detector, introducing large systematic errors.

For our global analysis, we used the SPOC 2 minutes light curve for the sector 34 transit, but we reextracted the 30 minutes FFI light curves for sectors 6 and 8 using a custom FFI pipeline based on the procedure described by Vanderburg et al. (2019). In brief, we performed aperture photometry on a series of 20 apertures, decorrelated each extracted light curve against the background flux outside the aperture and the mean value and standard deviation of pointing excursions during each exposure (measured from the spacecraft quaternion time series), and selected the light curve from the aperture that maximized photometric precision. We then removed any long-term instrumental and stellar variability signals by fitting a spline to the flux using *Keplerspline*³¹ and then dividing the light curve by the best-fit model (Vanderburg & Johnson 2014). We then removed most of the out-of-transit baseline from both light curves keeping only half a transit duration on each side of the transit since these data provide little to no information to the global fit while simultaneously being computationally expensive to model. These light curves were fit simultaneously with all available data on the HIP 33609 system (see Section 4.1).

2.2. Ground-based Photometric Follow Up

In order to rule out contamination by a background eclipsing binary and refine the ephemeris, we observed HIP 33609 as a part of SubGroup 1 (seeing limited photometry) of TFOP. We obtained these observations using the Las Cumbres Observatory Global Telescope (LCOGT) telescope network (Brown et al. 2013) and the 40 cm ASTEP-400 telescope (Abe et al. 2013; Guillot et al. 2015). Both facilities confirm the existence of a transit on the target star, HIP 33609, and confirm that there are no nearby stars that exhibit variability.

We observed an ingress of HIP 33609 b on 2020 December 8 UT from LCOGT-SSO on the 1 m telescope in the *y* band at 25 s cadence with a pixel scale of $0''.389$. We observed an egress on 2020 August 12 UT and a full transit (save for a brief gap midtransit due to a brief noon twilight) on 2021 June 23 UT with ASTEP using a 25 s exposure time with a pixel scale of $0''.93$. More transit observations were attempted by LCOGT and ASTEP, however they were at too low S/N to provide value to our global fit while increasing the computational cost. We therefore discard these transits and only show the three ground-based transits used in our analysis. We reduced these data sets and extracted the light curves using *AstroImageJ* (Collins et al. 2017). We detrended the LCO light curve against air mass and detrended the ASTEP light curves against both air mass and sky/pixels. See Section D in the appendix of Collins et al. (2017) for a detailed description of the detrending parameters.

2.3. CHIRON Spectroscopy

We observed HIP 33609 on 39 separate nights from 2020 January 24 UT through 2021 November 2 UT (Table 2) using

³⁰ <https://heasarc.gsfc.nasa.gov/docs/tess/the-tess-extended-mission.html>

³¹ <https://github.com/avanderburg/keplerspline>

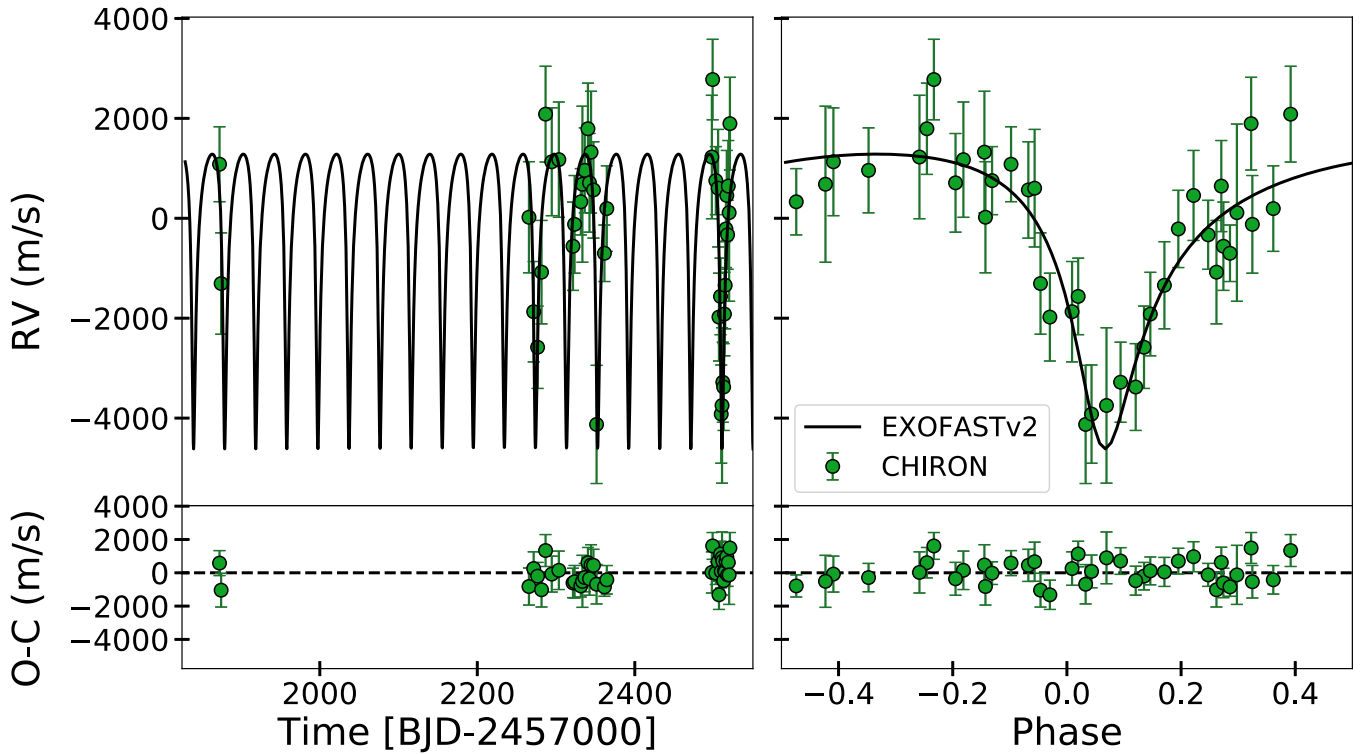


Figure 3. The radial velocity observations from CHIRON unphased (left) and phased to our best-fit ephemeris (right).

the CHIRON spectrograph on the 1.5 m SMARTS telescope located at the Cerro Tololo Inter-American Observatory in Chile (Tokovinin et al. 2013; Paredes et al. 2021). CHIRON is a high-resolution echelle spectrograph fed with an image slicer through a single multimode fiber, which achieves a spectral resolving power of $R = 80,000$ over the range 410–870 nm. We used these spectra to constrain the stellar parameters of the host star and extract the radial velocities (RVs). In order to extract the RVs, we derived the line profiles from our observed spectra by performing a least squares deconvolution (Donati et al. 1997; Zhou et al. 2020). We deconvolved against synthetic spectral templates generated using the ATLAS9 model atmospheres (Kurucz 1992) with our rotational broadening kernel applied.

We measured the projected rotational velocity $v \sin i_*$ of the host star by modeling the line profiles from our spectra with a convolution of kernels as prescribed by Zhou et al. (2018). They consisted of rotation and radial-tangential macroturbulence kernels from Gray (2005) and an instrumental broadening kernel which is represented as a Gaussian with a width equivalent to the instrumental resolution. From this analysis, we found that HIP 33609 has a projected rotational velocity of $v \sin i_* = 55.6 \pm 1.8 \text{ km s}^{-1}$. We constrained the stellar atmospheric parameters such as metallicity and effective temperature by comparing our spectra to an interpolated library of spectra classified by the stellar parameter classification package (Buchhave et al. 2012). However, we only utilized this analysis as a consistency check as determining stellar parameters through spectra is highly uncertain for rapidly rotating B-type stars like HIP 33609 (Gaudi et al. 2017). Therefore, we adopt the stellar parameters derived in our global fit, which are constrained by simultaneously fitting to the SED and stellar isochrones.

2.4. Spectral Energy Distribution

We fit the broadband SED simultaneously as a part of our global EXOFASTv2 analysis (see Section 4.1). However, we also performed a separate analysis of the SED in order to independently determine the basic stellar parameters and serve as a consistency check for our global analysis. We analyzed the SED of the star together with the Gaia DR3 parallax (with no systematic offset applied; see, e.g., Stassun & Torres 2021), in order to determine an empirical measurement of the stellar radius, following the procedures described in Stassun & Torres (2016), Stassun et al. (2017), and Stassun & Torres (2018). We pulled the $B_T V_T$ magnitudes from *Tycho-2*, the JHK_S magnitudes from *2MASS*, the W1–W4 magnitudes from WISE, and the $G G_{BP} G_{RP}$ magnitudes from Gaia. We also used the UV measurements at 157–274 nm from the TD1 UV satellite (Boksenberg et al. 1973; Thompson et al. 1995). Together, the available photometry spans the full stellar SED over the wavelength range 0.15–22 μm (see Figure 4).

We performed a fit to the SED using Kurucz stellar atmosphere models, with the main parameters being the effective temperature (T_{eff}), surface gravity ($\log g$), and metallicity ($[\text{Fe}/\text{H}]$), for which we adopted the spectroscopically determined values: $T_{\text{eff}} = 10,570^{+850}_{-710}$, $\log g = 4.259^{+0.057}_{-0.063}$, $[\text{Fe}/\text{H}] = -0.26^{+0.38}_{-0.61}$. The remaining free parameter was the extinction A_V , which we limited to the maximum line-of-sight value from the Galactic dust maps of Schlegel et al. (1998). The resulting fit has a reduced χ^2 of 1.5 and best-fit $A_V = 0.20 \pm 0.03$. Integrating the model SED gives the bolometric flux at Earth, $F_{\text{bol}} = 5.12 \pm 0.24 \times 10^{-8} \text{ erg s}^{-1} \text{ cm}^{-2}$. Taking the F_{bol} and T_{eff} together with the Gaia parallax yields the stellar radius, $R_* = 1.81 \pm 0.27 R_\odot$. In addition, we used the empirical relations of Torres et al. (2010), to estimate the stellar mass $M_* = 2.38 \pm 0.14 M_\odot$, which is

consistent with the value of $2.18 \pm 0.66 M_{\odot}$ determined empirically via R_* and $\log g$.

Finally, we can extrapolate the model atmosphere below 0.1 nm (see Stassun & Torres 2016) to estimate the XUV radiation in the BD's environment, for which we find $F_{\text{XUV}} = 302^{+532}_{-208} \text{ erg s}^{-1} \text{ cm}^{-2}$ at a distance of 1 au from the star. Overall, we find this analysis is consistent at the 1σ level with the results of our global analysis, and so we adopt the results of our EXOFASTv2 fit since it simultaneously fits all available data.

2.5. High-resolution Imaging

If an exoplanet host star has a spatially close companion, that companion (bound or line of sight) can create a false- positive transit signal if it is, for example, an eclipsing binary. The flux from a close companion star constitutes ‘‘third-light’’ and may lead to an underestimated planetary radius if not accounted for in the transit model (Ciardi et al. 2015) and cause nondetections of small planets in the same exoplanetary system (Lester et al. 2021). Additionally, the discovery of close, bound companion stars, which exist in nearly one-half of FGK type stars (Matson et al. 2018), provides crucial information toward our understanding of exoplanetary formation, dynamics and evolution (Howell et al. 2021). Thus, to search for close-in bound companions unresolved in TESS observations, we obtained high-resolution imaging speckle observations of HIP 33609.

HIP 33609 was observed on 2022 March 03 UT using the Zorro speckle instrument on the Gemini South 8 m telescope (Scott et al. 2021; Howell & Furlan 2022). Zorro provides simultaneous speckle imaging in two bands (562 nm and 832 nm) with output data products including a reconstructed image with robust contrast limits on companion detections. Three sets of 1000×0.06 s exposures were collected on HIP 33609 and subjected to Fourier analysis in our standard reduction pipeline (see Howell et al. 2011). Figure 4 shows our final contrast curves and the two reconstructed speckle images. We find that HIP 33609 is a single star with no companion brighter than 5–9 mag below that of the target star from the diffraction limit (20 mas) out to $1''.2$. At the distance of HIP 33609 ($d = 154$ pc) these angular limits correspond to spatial limits of 3–185 au.

We also observed HIP 33609 on 2019 May 18 UT from the 4.1 m Southern Astrophysical Research telescope with speckle interferometry in the I -band (Tokovinin 2018). We took these observations in line with the general observing strategy for TESS targets described in Ziegler et al. (2020) with an estimated contrast of $\Delta\text{mag} = 7.7$ at $1''$. We found no nearby companions out to $3''$.

3. Membership and Age Determination of HIP 33609

3.1. MELANGE-6

We searched for evidence that HIP 33609 is a member of a young stellar association using the FriendFinder³² (Tofflemire et al. 2021). FriendFinder used Gaia DR3 positions and parallaxes to identify all sources that fell within our selected three-dimensional search radius around HIP 33609. It then calculated the predicted tangential velocity (v_{tan}) for every nearby source assuming they have an identical UVW as the source. FriendFinder then compared that value to the true v_{tan} , derived from the Gaia proper motions. For this grouping, we selected targets with separation < 25 pc and a

Table 1
Literature and Measured Properties for HIP 33609

Other identifiers			
	TOI-588		
	TIC 130415266		
	HD 52470		
	HIP 33609		
	TYC 8122-01924-1		
	2MASS J06585996-4701240		
	TESS Sector	[6, 8, 33, 34, 35*]	
Parameter	Description	Value	Reference
α_{J2000} ^a	R.A. (R.A.)	06:58:59.966	1
δ_{J2000} ^b	decl. (Decl.)	−47:01:24.121	1
G	Gaia G mag.	7.26 ± 0.02	1
B_P	Gaia B_P mag.	7.27 ± 0.02	1
R_P	Gaia R_P mag.	7.30 ± 0.02	1
T	TESS mag.	7.312 ± 0.006	2
B_T	Tycho B_T mag.	7.271 ± 0.02	3
V_T	Tycho V_T mag.	7.284 ± 0.02	3
J	2MASS J mag.	7.245 ± 0.020	4
H	2MASS H mag.	7.326 ± 0.031	4
K_S	2MASS K_S mag.	7.278 ± 0.027	4
WISE1	WISE1 mag.	7.263 ± 0.036	5
WISE2	WISE2 mag.	7.326 ± 0.030	5
WISE3	WISE3 mag.	7.354 ± 0.030	5
WISE4	WISE4 mag.	7.4 ± 0.1	5
μ_{α}	Gaia DR3 proper motion in R.A. (mas yr^{-1})	-9.505 ± 0.073	1
μ_{δ}	Gaia DR3 proper motion in DEC (mas yr^{-1})	-4.467 ± 0.071	1
$v \sin i_*$	Rotational velocity (km s^{-1})	55.6 ± 1.8	Section 2.3
π ^b	Gaia DR3 parallax (mas)	6.49 ± 0.05	1

Notes. The uncertainties of the photometry have a systematic error floor applied.

^a R.A. and decl. are in epoch J2000. The coordinates come from Vizier where the Gaia R.A. and decl. have been precessed and corrected to J2000 from epoch J2015.5.

^b Values have been corrected for the $-0.30 \mu\text{as}$ offset as reported by Lindegren et al. (2018) but this is not significant for these systems.

References. (1) Gaia Collaboration et al. (2022), (2) Høg et al. (2000), (3) Stassun et al. (2018), (4) Cutri et al. (2003), (5) Cutri & Wright (2012).

difference in predicted and measured v_{tan} of $< 5 \text{ km s}^{-1}$. A larger physical search radius yielded more objects consistent with membership, but the narrow selection was more than sufficient for aging the star and demonstrating the existence of an association.

Our selection yielded 283 stars, including HIP 33609. The population color–magnitude diagram (CMD) followed a tight Pleiades-like sequence (Figure 5). Further, a high fraction of the candidate comovers had Gaia radial velocities consistent with HIP 33609. Importantly, FriendFinder did not use radial velocities or CMD information for selection, so consistency here made it clear this is a true comoving and coeval population. We denoted this population MELANGE-6, following the convention from Tofflemire et al. (2021).

³² <https://github.com/adamkraus/comove>

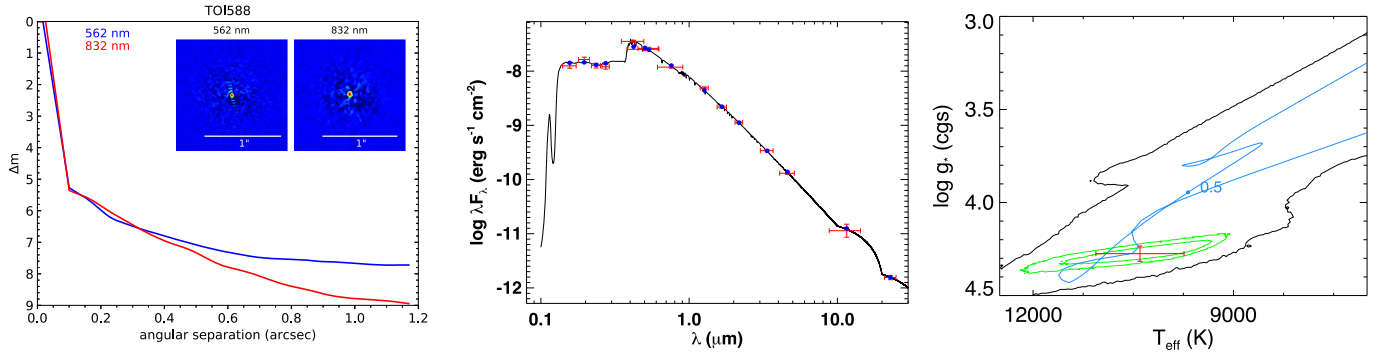


Figure 4. (Left) The 5σ speckle imaging contrast curves in both filters as a function of the angular separation from the diffraction limit (20 mas) out to $1''/2$, the end of speckle coherence. The inset shows the reconstructed 562 nm and 832 nm images with a $1''$ scale bar. HIP 33609 was found to have no close companions to within the angular and contrast levels achieved. (Middle) Spectral energy distribution of HIP 33609. Red symbols represent the observed photometric measurements, where the horizontal bars represent the effective width of the passband. Blue symbols are the model fluxes from the best-fit Kurucz atmosphere model (black). (Right) The best-fitting MESA Isochrones and Stellar Tracks (MIST) evolutionary track shown in blue with the 3σ contours on the best-fit MIST track in black. The red point indicates the median value and 1σ error bars from our global analysis, while the green contours show the 3σ errors. The blue point indicates the location of 0.5 Gyr on the evolutionary track.

Table 2
The Radial Velocity Measurements for the HIP 33609 System

BJD _{TDB}	RV (m s ⁻¹)	σ_{RV} (m s ⁻¹)	BJD _{TDB}	RV (m s ⁻¹)	σ_{RV} (m s ⁻¹)
2458872.64968	32201.9	769.6	2459364.44268	31314.1	873.7
2458874.68716	29813.7	1029.1	2459497.86645	32346.2	1247.6
2459265.59795	31140.8	1125.7	2459498.86337	33896.8	823.9
2459271.58653	29249.9	1019.7	2459502.88700	31873.6	702.7
2459276.56080	28538.2	842.3	2459505.82903	31722.4	1189.3
2459281.57067	30041.5	1049.7	2459506.88278	29142.3	896.2
2459286.69996	33204.2	974.2	2459508.84044	29556.2	785.5
2459294.55752	32251.1	1093.2	2459509.76436	27200.5	998.3
2459303.54558	32293.7	1167.0	2459510.79825	27373.0	1564.7
2459321.52137	30560.4	900.5	2459511.77084	27838.5	820.2
2459323.52343	30998.6	992.5	2459512.81732	27742.1	886.0
2459331.46144	31450.3	685.8	2459513.82850	29202.6	853.4
2459333.48087	31801.6	1571.2	2459514.80241	29779.1	889.0
2459336.46010	32079.4	868.0	2459515.76514	30906.6	792.1
2459340.49478	32912.0	930.0	2459516.81742	31576.8	917.3
2459342.47356	31829.6	1002.2	2459517.82665	30789.3	711.5
2459344.46994	32443.8	1230.7	2459518.73563	31764.7	927.9
2459347.50808	31687.2	979.7	2459519.81360	31232.3	1781.9
2459351.46803	26993.6	1195.5	2459520.79849	33014.2	944.1
2459361.44832	30419.7	591.6			

3.2. Measuring MELANGE-6's Age

To determine the age of MELANGE-6 (and hence the age of HIP 33609) we first compared the Gaia magnitudes to model isochrones following Mann et al. (2022). To briefly summarize, we used a mixture model as outlined in Hogg et al. (2010). The mixture contained two models, one for the single-star coeval population, and an outlier population to account for non-members and binaries, inclusion of which tends to bias the isochronal age to older or younger ages, respectively. The fit was done in an MCMC framework using `emcee` (Foreman-Mackey et al. 2013). The six free parameters were age (τ), reddening ($E(B-V)$ [mags]), the amplitude of the outlier population (P_B), the offset from the main population to the outlier population (Y_B [mags]), the variance in the outlier population (V_B) and a parameter to account for underestimated uncertainties or differential reddening (f [mags]).

We tested fits using the PARSECv1.2 (Bressan et al. 2012) and the Dartmouth Stellar Evolution Program (DSEP; Dotter et al. 2008) with magnetic enhancement (Feiden & Chaboyer 2012).

We initially restricted our analysis to Solar metallicity, but tested $[M/H] = -0.1$ and $+0.1$ with the PARSEC models. The DSEP-magnetic models were only available at Solar metallicity and did not extend to the highest-mass stars in the group. We ran the fit with 20 walkers for 10,000 steps following a burn-in of 2000 steps, which was >50 times the autocorrelation time.

As we show in Figure 5, ages $\gtrsim 200$ Myr or < 80 Myr failed to reproduce the pre-main-sequence M dwarfs. The isochrone fit yielded an age of 106_{-8}^{+11} Myr, with negligible reddening ($E(B-V) < 0.05$) and a small outlier population ($P_B = 0.15 \pm 0.05$). The errors on the age are likely underestimated due to our assumptions and limitations of the models. For example, a slightly metal-rich grid ($[M/H] = +0.1$) gave a similar fit and yielded an older age 118_{-8}^{+12} Myr. Additional adjustments, such as down weighting the coolest stars, where models struggle to reproduce observations, changed the age at the 10 Myr level.

As an additional constraint on age, we also measured rotation periods for candidate members of MELANGE-6 from their TESS light curves. The rotation sequence provides an age

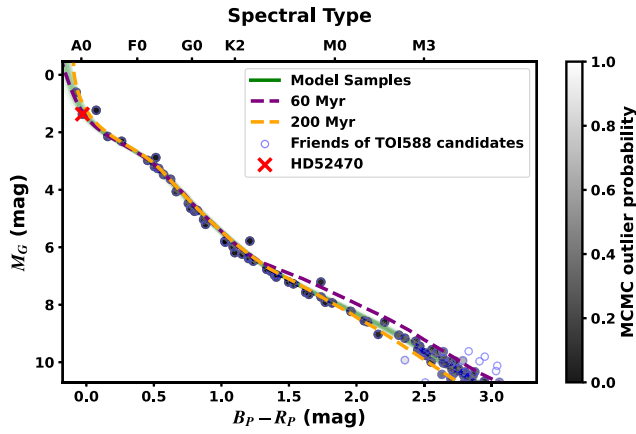


Figure 5. Color–magnitude diagram (CMD) of stars spatially and kinematically near HIP 33609. The green lines show random draws from our MCMC fit posterior. Points are shaded by the probability that they are part of the outlier model. HIP 33609 is denoted with a red X. The orange and purple lines designate age extremes for reference.

constraint that is (largely) independent of the isochronal measurement, instead relying on the relation between age, color, and rotation period (Gyrochronology; Barnes 2003).

We followed the method outlined in Barber et al. (2022). To briefly summarize, we generated TESS light curves from the FFI cutouts, first creating raw flux light curves from the FFI cutouts centered on each candidate. Then, we generated a Causal Pixel Model (CPM) of the telescope systematics using the `unpopular` package (Hattori et al. 2022) using the “Similar Brightness” to generate the model for each star. We subtracted the resulting CPM systematic model from the initial light curves. In total, we extracted usable light curves for 117 targets; the majority of the remaining were too faint or had significant contaminating flux from nearby stars.

We searched every single-sector light curve for each star for rotation periods from 0.1–30 days using the Lomb–Scargle algorithm (Lomb 1976). Each identified period was inspected by eye and assigned a quality score following Rampalli et al. (2021) with an additional quality flag of -99 for stars with no data or stars beyond TESS rotation period detection limits (TESS mag >15 or contamination ratio >1.6). We retained periods with a score of Q0 or Q1 (105 stars).

We show the rotation sequence in Figure 6. The slowly rotating sequence of FGK dwarfs in MELANGE-6 sits above the Pleiades (Rebull et al. 2016), indicating an age >112 Myr (Dahm 2015). The sequence also closely matches that of Theia 456 (Kounkel & Covey 2019), which was recently determined to be 150–200 Myr (Andrews et al. 2022).

The gyrochronological age is somewhat older than our isochronal value. However, the systematics in the isochronal age were sufficient that the measurements are consistent. We adopted a generous age of 150 ± 25 Myr which encompasses both estimates.

4. Analysis

4.1. EXOFASTv2 Global Fits

We globally fit all available data using the public exoplanet fitting suite EXOFASTv2 (Eastman et al. 2013, 2019) in order to determine the host star and companion parameters for the HIP 33609 system (Tables 3 and 4). We fit the SED and used the MIST stellar evolution models (Paxton et al. 2011, 2013, 2015;

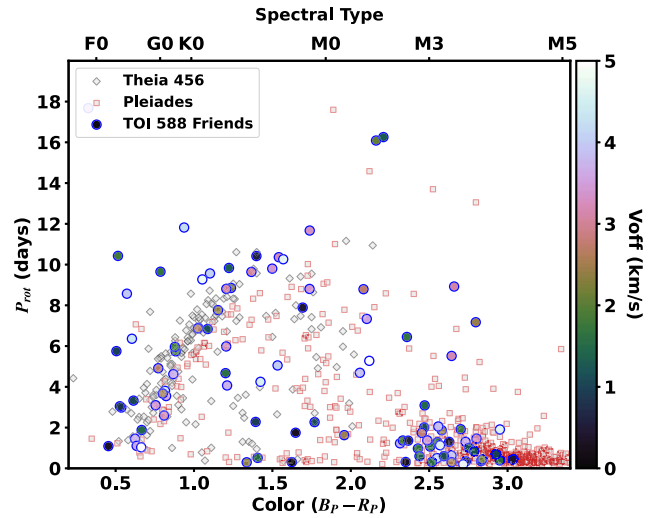


Figure 6. Rotation periods of candidate members of MELANGE-6 as a function of $B_p - R_p$ color. The rotation periods show a clear sequence as expected for a coeval association, and the outliers tend to be further from HIP 33609 kinematically (see color coding). We show the sequences for Theia 456 (150–200 Myr Andrews et al. 2022) and Pleiades (112 Myr Rebull et al. 2016) for comparison.

(The data used to create this figure are available.)

Choi et al. 2016; Dotter 2016) in order to constrain the parameters of the host star. We account for smearing from the 30 minutes cadence in our FFI light curves from sectors 6 and 8. Our ground-based photometric follow up from both LCOGT and ASTEP were additively detrended against the parameters described in Section 2.2 (Collins et al. 2017).

We initially exclude all ground-based transits from the fit, incorporating only the TESS transits, CHIRON radial velocities, and the SED. We turn off the Claret (Claret 2017) tables for these fits since they are less reliable for hot stars ($>10,000$ K) and allow the fit to constrain the quadratic limb-darkening coefficients directly from the TESS transits. The TESS 30 minutes and 2 minutes light curves have out-of-transit standard deviations of 110 ppm and 310 ppm, respectively, which was precise enough to independently constrain the limb-darkening coefficients in the TESS bandpass. We then add in each ground-based transit iteratively, ensuring that each successive fit is still consistent with the TESS only fit to 1σ . Since the ground-based light curves have too low S/N to constrain limb darkening in their respective bandpasses, we apply Gaussian priors on the limb-darkening coefficients according to the methods suggested by Patel & Espinoza (2022). The results presented in Tables 3, and 4 are the final iterations of this process including all ground-based light curves discussed in Section 2.2.

We adopted the age, as discussed in Section 3, of 150 ± 25 Myr as a Gaussian prior in our global fits, and placed a Gaussian prior on the parallax from Gaia DR3 (Gaia Collaboration et al. 2022) while correcting for the parallax bias according to Lindegren et al. (2021). We also placed an upper limit on the line-of-sight extinction as described in Schlegel et al. (1998) and Schlafly & Finkbeiner (2011). Because HIP 33609 is a rapidly rotating B star, stellar parameters derived from spectroscopic observations are not reliable. Therefore, we do not obtain precise measurements for the stellar metallicity from our spectral analysis and thus set a Gaussian prior of

Table 3

Median Values and 68% Confidence Interval for Global Model of HIP 33609

Stellar Parameters:		
M_*	Mass (M_\odot)	$2.383^{+0.10}_{-0.095}$
R_*	Radius (R_\odot)	$1.863^{+0.087}_{-0.082}$
F_{Bol}	Bolometric flux (cgs)	$0.0000000497^{+0.0000000014}_{-0.0000000097}$
ρ_*	Density (cgs)	$0.519^{+0.076}_{-0.065}$
$\log g$	Surface gravity (cgs)	$4.274^{+0.042}_{-0.040}$
T_{eff}	Effective temperature (K)	10400^{+800}_{-660}
[Fe/H]	Metallicity (dex)	$-0.01^{+0.19}_{-0.20}$
[Fe/H] ₀	Initial metallicity ^a	$0.02^{+0.18}_{-0.20}$
Age	Age (Gyr)	0.153 ± 0.024
EEP	Equal evolutionary phase ^b	$314.3^{+7.3}_{-7.4}$
A_V	V-band extinction (mag)	$0.134^{+0.075}_{-0.084}$
σ_{SED}	SED photometry error scaling	$1.28^{+0.38}_{-0.26}$
ϖ	Parallax (mas)	6.483 ± 0.049
d	Distance (pc)	154.3 ± 1.2
Planetary Parameters:		
P	Period (days)	39.471814 ± 0.000014
R_p	Radius (R_J)	$1.580^{+0.074}_{-0.070}$
M_p	Mass (M_J)	$68.0^{+7.4}_{-7.1}$
T_C	Time of conjunction (BJD _{TDB})	$2459231.75856 \pm 0.00021$
T_0	Optimal conjunction time ^c (BJD _{TDB})	$2458915.98404 \pm 0.00017$
a	Semimajor axis (au)	$0.3058^{+0.0042}_{-0.0041}$
i	Inclination (degrees)	89.13 ± 0.15
e	Eccentricity	$0.560^{+0.029}_{-0.031}$
ω_*	Argument of periastron (degrees)	$165.9^{+5.5}_{-5.6}$
T_{eq}	Equilibrium temperature (K)	1237^{+73}_{-61}
τ_{circ}	Tidal circularization time-scale ^d (Gyr)	9800^{+6300}_{-4000}
K	RV semiamplitude (m s^{-1})	2700 ± 290
R_p/R_*	Radius of planet in stellar radii	$0.08715^{+0.00034}_{-0.00036}$
a/R_*	Semimajor axis in stellar radii	$35.3^{+1.6}_{-1.5}$
τ	Ingress/egress transit duration (days)	$0.02401^{+0.00088}_{-0.00089}$
T_{14}	Total transit duration (days)	0.26960 ± 0.00080
b	Transit impact parameter	$0.328^{+0.042}_{-0.053}$
$T_{S,14}$	Total eclipse duration ^e (days)	$0.341^{+0.031}_{-0.028}$
ρ_p	Density (cgs)	$21.3^{+4.0}_{-3.4}$
$\log g_p$	Surface gravity	$4.829^{+0.059}_{-0.062}$
$\langle F \rangle$	Incident flux ($10^9 \text{ erg s}^{-1} \text{ cm}^{-2}$)	$0.398^{+0.11}_{-0.075}$
T_S	Time of eclipse (BJD _{TDB})	$2459238.47^{+0.75}_{-0.68}$
$e \cos \omega_*$		$-0.541^{+0.037}_{-0.034}$
$e \sin \omega_*$		$0.136^{+0.050}_{-0.051}$
d/R_*	Separation at midtransit	$21.3^{+2.3}_{-2.0}$

Notes. See Table 3 in Eastman et al. (2019) for a list of the derived and fitted parameters in EXOFASTv2.

^a Initial metallicity is the metallicity of the star when it formed.

^b The equal evolutionary point is a proxy for age and corresponds to static points in a stars evolution when using MIST isochrones. See Section 2 in Dotter (2016) for a more detailed description of EEP.

^c Transit midpoint time that minimizes the covariance between TC and Period.

^d The tidal quality factor (Q_p) is assumed to be 10^6 .

^e All values in this table for the secondary occultation of HIP 33609 b are predicted values from our global analysis.

0.0 ± 0.5 dex. We also set a Gaussian prior of $0\% \pm 10\%$ of the contamination ratio reported in the TESS Input Catalogue (TIC; Stassun et al. 2018) in order to fit for a dilution term in the TESS band. While the SPOC PDC-SAP light curves are corrected for known nearby companions, fitting for a dilution term accounts for unknown nearby blended stars in the TESS

aperture and serves as an independent check on the reported contamination correction. We adopted the convergence criteria of Eastman et al. (2019) which recommend a Gelman–Rubin statistic < 1.01 and over 1000 independent draws.

4.2. Gravity-darkening Fit

Given that HIP 33609 is a rapidly rotating B star, we expect that gravity darkening would have a significant effect on the light curve (Barnes 2009). Hence, we performed two additional fits in order to investigate the effects of gravity darkening on HIP 33609’s light curve. We perform a symmetric fit based on the standard Mandel & Agol (2002) transit model as well as an additional, similar fit following the techniques described in Hooton et al. (2022) in order to account for deviations induced by oblateness and brightness variations that arise from gravity darkening (see Figure 7). For this analysis, we fit only the transits from TESS because of the much lower signal to noise ratios of the ground-based light curves, as well as the fact that systematics in ground-based observations can imitate the effects of gravity darkening.

In both fits, we adopted Gaussian priors based on the EXOFASTv2 outputs where possible. We reparameterized the limb-darkening coefficients u_1 , u_2 taken directly from the Claret (2017) tables according to Kipping (2013) and adopted Gaussian priors with standard deviations of 0.5 and 0.1, respectively. We used wide uniform priors on the period, time of conjunction, and planetary radius in addition to a uniform prior ranging from -1 to 1 on $\sqrt{e} \cos \omega$ and $\sqrt{e} \sin \omega$. We also used a wide uniform prior on the impact parameter b for both fits. However, in the case of the gravity-darkening fit, we allowed b to also sample negative values as we can no longer assume a symmetric stellar disk. Finally, we fixed the gravity-darkening exponent β according to Claret (2017).

We found that both of these fits are in good agreement with our global EXOFASTv2 fit as all parameters commonly fit among the three methods agreed within 2 sigma. We found no significant asymmetries induced by gravity darkening, and therefore we adopt the results from our global EXOFASTv2 fit. While our gravity darkening fit is unable to strongly constrain the alignment, the fit favors a potential large misalignment. We encourage additional characterization through Doppler tomography or Rossiter–McLaughlin techniques in order to further constrain the orbital architecture of the HIP 33609 system.

4.3. CEPAM Evolutionary Models

Using CEPAM (Guillot & Morel 1995), we calculate evolutionary tracks of HIP 33609 b. Our models are based on the same approach as in Bouchy et al. (2011), using the analytical atmospheric boundary conditions from Guillot (2010). Our fiducial model has a solar metallicity interior ($Z_{\text{interior}}^* = Z_\odot$) and thermal and visible mean opacities set to $\kappa_{\text{th}}^* = 0.04 \text{ g cm}^{-2}$ and $\kappa_{\text{v}}^* = 0.024 \text{ g cm}^{-2}$, respectively. As shown in Figure 8, this model reproduces the observed radius for the age of HIP 33609 b. Because of the brown dwarf’s large mass and intrinsic luminosity ($L_{\text{int}} = 4 \times 10^{30} \text{ erg s}^{-1}$), we find that the interior is entirely convective and therefore its evolution is not affected by changes of the interior opacities. The energy supplied by tidal dissipation, $L_{\text{tides}} \approx 10^{25} \text{ erg s}^{-1}$ for a tidal quality factor ($Q' = 10^6$) (e.g., Bodenheimer et al. 2001), is also too low to affect the evolution, as is that due to

Table 4
Median Values and 68% Confidence Interval for Global Model of HIP 33609

Wavelength Parameters		R	z'	TESS
u_1	Linear limb-darkening coeff	$0.043^{+0.061}_{-0.032}$	$0.043^{+0.061}_{-0.032}$	0.359 ± 0.050
u_2	Quadratic limb-darkening coeff	$0.032^{+0.078}_{-0.046}$	$0.044^{+0.084}_{-0.054}$	$-0.050^{+0.089}_{-0.086}$
A_D	Dilution from neighboring stars	0.0001 ± 0.0016
Telescope Parameters		CHIRON		
γ_{rel}	Relative RV offset (m s^{-1})	31130 ± 150		
σ_J	RV jitter (m s^{-1})	$0.00^{+400}_{-0.00}$		
σ_J^2	RV jitter variance	$-30000^{+190000}_{-130000}$		
Transit Parameters:		TESS (30 minute)	TESS (2 minute)	
σ^2	Added variance	$0.0000000045^{+0.0000000022}_{-0.0000000017}$	$0.0000000016^{+0.0000000055}_{-0.0000000051}$	
F_0	Baseline flux	1.000011 ± 0.000014	1.000045 ± 0.000014	

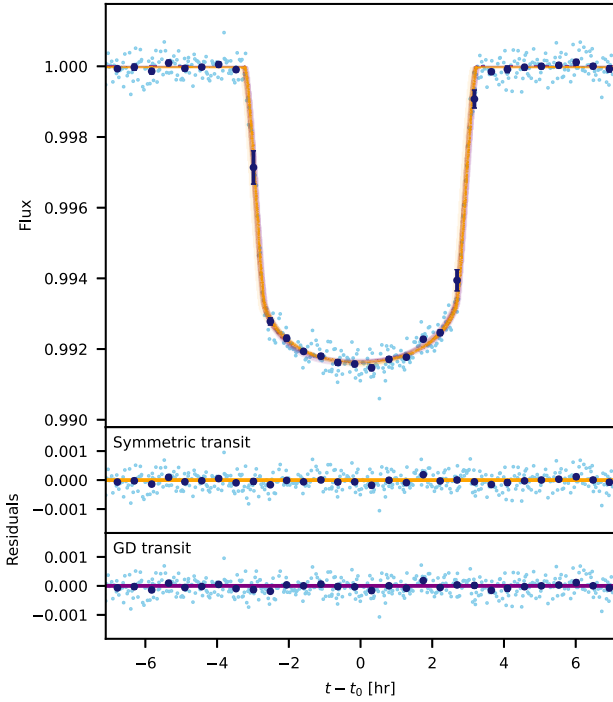


Figure 7. (Top) The TESS transits for HIP 33609 b phase-folded and binned to 30 minutes. 32 independent draws from the posteriors of the symmetric Mandel & Agol (2002) fit are plotted in orange, and 32 independent draws from the gravity darkening fit (Hooton et al. 2022) are plotted in purple (see Section 4.2). While the median models are very similar between the two fits, we note the slight asymmetries seen in the gravity-darkening posteriors hint at a potential misalignment.

internal dissipation $L_{\text{dissipation}} \approx 10^{27} \text{ erg s}^{-1}$ (see Thorngren & Fortney 2018).

The radius of HIP 33609 b is thus mainly affected by three factors: the initial formation entropy (here we assume a hot start initial entropy of $S = 13.4 k_B/\text{baryon}$), the deep interior mean molecular weight and the atmospheric opacity (see Guillot 2005). Figure 8 shows that the latter is by far the dominant effect: when multiplying the atmospheric opacities by 2 over their fiducial values, we obtain a theoretical radius that is 25% larger (at the measured age) than our fiducial model and clearly incompatible with the observations. On the other hand, when multiplying the interior metallicity by a factor 5 (equivalent to adding $4.2 M_{\text{Jup}}$ of heavy elements in its interior) the radius change remains limited. Although a wider ensemble

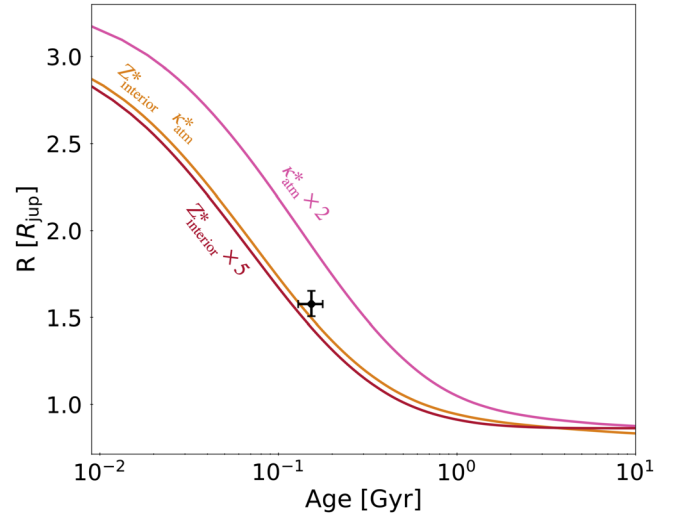


Figure 8. The radius evolution of HIP 33609 b. The black point signifies the measured age and radius with 1σ error bars. The orange line is our fiducial evolutionary model (see Section 4.3). The pink line multiplies the atmospheric opacities of the fiducial model by 2, and the red line multiplies the interior metallicity by 5.

of dedicated evolution models should be calculated, this already shows that observations of HIP 33609 b with the James Webb Space Telescope would be extremely important, by independently yielding its atmospheric metallicity (that we predict should be solar) and intrinsic luminosity (our evolution models predict $T_{\text{eff}} = 2630 \text{ K}$).

5. Discussion

HIP 33609 b joins a population of 37 transiting BDs published to date (Grieves et al. 2021; Carmichael et al. 2022; Psaridi et al. 2022; Sebastian et al. 2022), and is one of the most extreme substellar companions yet discovered. HIP 33609 not only has a precise age measurement of $150 \pm 25 \text{ Myr}$, but is also the brightest and hottest host of a transiting BD discovered to date. The unique combination of host star and BD parameters (see Figure 9) make the HIP 33609 system a benchmark for testing theories of substellar evolution, BD orbital dynamics, and the effects of insolation on BD atmospheres.

The HIP 33609 system also extends our knowledge of transiting companions around hot stars. All previously discovered transiting companions around B- and A-type stars

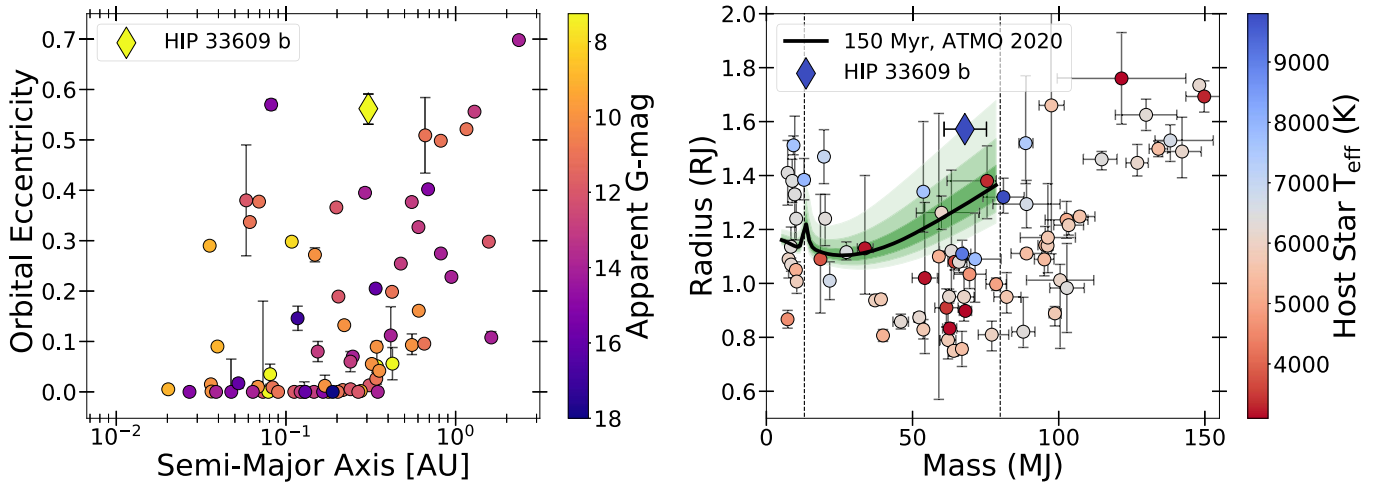


Figure 9. (Left) The population of stellar companions ranging from 7–150 M_J in eccentricity and semimajor axis, colored by the apparent magnitude. (Right) The same population in radius and mass, colored by the effective temperature of the host star. Vertical lines at 13 M_J and 80 M_J denote the traditional boundaries of the BD regime. The solid black line shows the ATMO 2020 substellar evolutionary model (Phillips et al. 2020) for HIP 33609 b’s measured age (150 ± 25 Myr) with the green shaded regions depicting the 1, 2, and 3σ uncertainties. Note: systems where the primary body is a BD or white dwarf are not included. References: Bakos (2010), Buchhave et al. (2011), Tingley et al. (2011), Parviainen et al. (2014), Bonomo et al. (2015), Esteves et al. (2015), Stassun et al. (2017), Bento et al. (2018), Cooke et al. (2020), Cortés-Zuleta et al. (2020), Grieves et al. (2021), Carmichael et al. (2022), Gill et al. (2022), Psaridi et al. (2022), Sebastian et al. (2022).

have orbital periods less than 10 days (Shporer et al. 2014; Morton et al. 2016; Gaudi et al. 2017; Lund et al. 2017; Talens et al. 2017; Anderson et al. 2018; Johnson et al. 2018; Hellier et al. 2019; Zhou et al. 2019; Dorval et al. 2020; Stevens et al. 2020; Addison et al. 2021; Giacalone et al. 2022), whereas HIP 33609 provides the first companion on a long-period orbit (~ 39 days).

5.1. Placing HIP 33609 in Context

HIP 33609 b orbits a bright ($V = 7.3$) B star with a precisely measured age, and joins a growing population of 12 BDs with host stars above the Kraft break (~ 6250 K, Kraft 1967), an exciting regime for studying BD evolution in the context of star-like versus planet-like formation. For example, if BDs do indeed follow formation and evolutionary pathways similar to the giant planets, then we can draw comparisons to recent studies focused on hot Jupiters that have observed a discontinuity in stellar obliquity at the Kraft break (Schlaufman 2010; Winn et al. 2010). Rice et al. (2022) suggest that this discontinuity may only exist for the low eccentricity population, a trend that would provide strong evidence for high-eccentricity migration as the dominant migration mechanism for hot Jupiters. This hypothesis is also supported by the current population of TESS discovered giant planets (Rodríguez et al. 2023; Yee et al. 2022). If BDs and giant planets undergo similar migratory processes, then they could exhibit the same discontinuity in stellar obliquity. HIP 33609 b’s high-eccentricity ($e = 0.560_{-0.031}^{+0.029}$) makes it the second most eccentric BD behind KOI-415 ($e = 0.698$) (Moutou et al. 2013). However, HIP 33609 is significantly more accessible to follow up because it is more than 500 times brighter than KOI-415 ($V = 14.2$).

Furthermore, HIP 33609 b’s radius is among the largest for transiting BDs at $R_b = 1.580_{-0.070}^{+0.074} R_J$. Substellar evolutionary models predict that BDs form highly inflated and then contract, rapidly at first, then slowing over the course of ~ 10 Gyr (Burrows et al. 2001; Baraffe et al. 2003; Saumon & Marley 2008; Phillips et al. 2020). HIP 33609 b’s large radius

is consistent within 3σ for substellar models at the estimated age from our analysis using both CEPAM (Figure 8) and the ATMO 2020 models (Figure 9).

5.2. Future Characterization Prospects

As the brightest and hottest host star for a transiting BD, the HIP 33609 system is well-situated for future characterization via ground-based observations. Although the long transit duration (~ 6.5 hours) will make spin-orbit alignment measurements challenging, HIP 33609 b would be a valuable addition to the population of BDs with well-constrained stellar obliquities.

We predict a Rossiter–McLaughlin semiamplitude to first order of 270 m s^{-1} for HIP 33609 b using the methods in Triaud (2018). While this is indeed well below our typical radial velocity uncertainty of $\sim 1000 \text{ m s}^{-1}$ with CHIRON, we expect orbital obliquity measurements to be more accessible to Doppler Tomographic techniques (Collier Cameron et al. 2010; Zhou et al. 2016) given that we can resolve the rotation of the host star. A finding that HIP 33609 b is highly misaligned, as tentatively indicated by our gravity-darkening fit, would provide strong evidence for a dynamically active history. We also encourage future measurements of more BD obliquities in general, in order to provide insight into BD evolutionary pathways similar to that obtained from the obliquity studies of hot Jupiters discussed in Section 5.1.

HIP 33609 b is also a prime candidate for studying the effects of insolation on BD and giant planet atmospheres. As a long-period, massive companion, it can thereby extend the extensive studies of the irradiated atmospheres of BDs and giant planets. The BD KELT-1 b (Siverd et al. 2012; Beatty et al. 2014; von Essen et al. 2021), and giant planets KELT-9 b (Gaudi et al. 2017; Hoeijmakers et al. 2018; Yan & Henning 2018) and TOI-1431 b (Stangret et al. 2021) are all ultrahot ($T_{\text{eq}} > 2000$ K) companions with well-studied atmospheres that receive approximately 10 times more incident flux than HIP 33609 b.

6. Conclusion

In this paper, we present the discovery of a benchmark transiting BD in the HIP 33609 system. We use a combination of spectroscopic and photometric observations from both ground- and space-based facilities in order to characterize the host star and transiting BD. HIP 33609 is a bright ($V=7.3$), rapidly rotating B star with an effective temperature of $T_{\text{eff}} = 10,400_{-660}^{+800}$ K. HIP 33609 b is an inflated BD with a radius of $R_b = 1.580_{-0.070}^{+0.074} R_J$ and a mass of $M_b = 68.0_{-7.1}^{+7.4} M_J$ on a long-period ($p = 39.47$ days), eccentric orbit ($e = 0.560_{-0.031}^{+0.029}$). We also present the discovery of MEL-ANGE-6, a new, young stellar association, of which HIP 33609 is shown to be a member. We determine the age of the association (and hence HIP 33609) to be 150 ± 25 Myr. Thus, the HIP 33609 system is an ideal candidate for testing substellar evolutionary models, as well as for a comparative analysis relative to the extensive population of highly irradiated, short period BDs and giant planets. We encourage the pursuit of stellar obliquity measurements for HIP 33609 b and the transiting BD population as a whole in order to provide more insight into the formation and evolutionary history of transiting BDs.

Some of the data presented in this paper were obtained from the Mikulski Archive for Space Telescopes (MAST) at the Space Telescope Science Institute. The specific observations analyzed can be accessed via DOI:10.17909/t9-nmc8-f686 and DOI:10.17909/0cp4-2j79.

A.W.M. was supported by a grant from NASA's Exoplanet research program (80NSSC21K0393). D.R. was supported by NASA under award number NNA16BD14C.

Resources supporting this work were provided by the NASA High-End Computing (HEC) Program through the NASA Advanced Supercomputing (NAS) Division at Ames Research Center for the production of the SPOC data products.

Funding for the TESS mission is provided by NASA's Science Mission Directorate. We acknowledge the use of public TESS data from pipelines at the TESS Science Office and at the TESS Science Processing Operations Center. This research has made use of the Exoplanet Follow-up Observation Program website, which is operated by the California Institute of Technology, under contract with the National Aeronautics and Space Administration under the Exoplanet Exploration Program. This paper includes data collected by the TESS mission that are publicly available from MAST. This research has made use of the NASA Exoplanet Archive, which is operated by the California Institute of Technology, under contract with the National Aeronautics and Space Administration under the Exoplanet Exploration Program.

This work makes use of observations from the LCOGT network. Part of the LCOGT telescope time was granted by NOIRLab through the Mid-Scale Innovations Program (MSIP). MSIP is funded by NSF.

This work makes use of observations from the ASTEP telescope. ASTEP benefited from the support of the French and Italian polar agencies IPEV and PNRA in the framework of the Concordia station program, from OCA, INSU, Idex UCAJEDI (ANR- 15-IDEX-01), the University of Birmingham, and ESA.














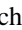

















Some of the observations in the paper made use of the High-Resolution Imaging instrument Zorro obtained under Gemini LLP Proposal Number: GN/S-2021A-LP-105. Zorro was

funded by the NASA Exoplanet Exploration Program and built at the NASA Ames Research Center by Steve B. Howell, Nic Scott, Elliott P. Horch, and Emmett Quigley. Zorro was mounted on the Gemini North (and/or South) telescope of the international Gemini Observatory, a program of NSF's OIR Lab, which is managed by the Association of Universities for Research in Astronomy (AURA) under a cooperative agreement with the National Science Foundation, on behalf of the Gemini partnership: the National Science Foundation (United States), National Research Council (Canada), Agencia Nacional de Investigación y Desarrollo (Chile), Ministerio de Ciencia, Tecnología e Innovación (Argentina), Ministério da Ciência, Tecnologia, Inovações e Comunicações (Brazil), and Korea Astronomy and Space Science Institute (Republic of Korea).

This research received funding from the European Research Council (ERC) under the European Union's Horizon 2020 research and innovation program (grant agreement No. 803193/BEBOP), and from the Science and Technology Facilities Council (STFC; grant No. ST/S00193X/1).

This work has been carried out within the framework of the NCCR PlanetS supported by the Swiss National Science Foundation under grants 51NF40_182901 and 51NF40_205606.

ORCID iDs

Noah Vowell  <https://orcid.org/0000-0002-0701-4005>
 Joseph E. Rodriguez  <https://orcid.org/0000-0001-8812-0565>
 Samuel N. Quinn  <https://orcid.org/0000-0002-8964-8377>
 George Zhou  <https://orcid.org/0000-0002-4891-3517>
 Andrew Vanderburg  <https://orcid.org/0000-0001-7246-5438>
 Andrew W. Mann  <https://orcid.org/0000-0003-3654-1602>
 Matthew J. Hooton  <https://orcid.org/0000-0003-0030-332X>
 Keivan G. Stassun  <https://orcid.org/0000-0002-3481-9052>
 Saburo Howard  <https://orcid.org/0000-0003-4894-7271>
 Allyson Bieryla  <https://orcid.org/0000-0001-6637-5401>
 David W. Latham  <https://orcid.org/0000-0001-9911-7388>
 Steve B. Howell  <https://orcid.org/0000-0002-2532-2853>
 Tristan Guillot  <https://orcid.org/0000-0002-7188-8428>
 Karen A. Collins  <https://orcid.org/0000-0001-6588-9574>
 Theron W. Carmichael  <https://orcid.org/0000-0001-6416-1274>
 Jon M. Jenkins  <https://orcid.org/0000-0002-4715-9460>
 Avi Shporer  <https://orcid.org/0000-0002-1836-3120>
 Lyu ABE  <https://orcid.org/0000-0002-0856-4527>
 Philippe Bendjoya  <https://orcid.org/0000-0002-4278-1437>
 Jonathan L. Bush  <https://orcid.org/0000-0002-9446-9250>
 Marco Buttu  <https://orcid.org/0000-0003-4559-049X>
 Kevin I. Collins  <https://orcid.org/0000-0003-2781-3207>
 Jason D. Eastman  <https://orcid.org/0000-0003-3773-5142>
 Matthew J. Fields  <https://orcid.org/0000-0002-9641-3138>
 Thomas Gasparetto  <https://orcid.org/0000-0002-7913-4866>
 Maximilian N. Günther  <https://orcid.org/0000-0002-3164-9086>
 Veselin B. Kostov  <https://orcid.org/0000-0001-9786-1031>
 Adam L. Kraus  <https://orcid.org/0000-0001-9811-568X>
 Kathryn V. Lester  <https://orcid.org/0000-0002-9903-9911>
 Alan M. Levine  <https://orcid.org/0000-0001-8172-0453>
 Colin Littlefield  <https://orcid.org/0000-0001-7746-5795>
 Djamel Mékarnia  <https://orcid.org/0000-0001-5000-7292>

David Rapetti  <https://orcid.org/0000-0003-2196-6675>
 George R. Ricker  <https://orcid.org/0000-0003-2058-6662>
 S. Seager  <https://orcid.org/0000-0002-6892-6948>
 Ramotholo Sefako  <https://orcid.org/0000-0003-3904-6754>
 Olga Suarez  <https://orcid.org/0000-0002-3503-3617>
 Guillermo Torres  <https://orcid.org/0000-0002-5286-0251>
 Amaury H. M. J. Triaud  <https://orcid.org/0000-0002-5510-8751>
 R. Vanderspek  <https://orcid.org/0000-0001-6763-6562>
 Joshua N. Winn  <https://orcid.org/0000-0002-4265-047X>

References

- Abe, L., Gonçalves, I., Agabi, A., et al. 2013, *A&A*, **553**, A49
 Addison, B. C., Knudstrup, E., Wong, I., et al. 2021, *AJ*, **162**, 292
 Anderson, D. R., Temple, L. Y., Nielsen, L. D., et al. 2018, arXiv:1809.04897
 Andrews, J. J., Curtis, J. L., Chanamé, J., et al. 2022, *AJ*, **163**, 275
 Baraffe, I., Chabrier, G., Allard, F., & Hauschildt, P. H. 2002, *A&A*, **382**, 563
 Baraffe, I., Chabrier, G., Barman, T. S., Allard, F., & Hauschildt, P. H. 2003, *A&A*, **402**, 701
 Barber, M. G., Mann, A. W., Bush, J. L., et al. 2022, *AJ*, **164**, 88
 Barnes, J. W. 2009, *ApJ*, **705**, 683
 Barnes, S. A. 2003, *ApJ*, **586**, 464
 Beatty, T. G., Collins, K. A., Fortney, J., et al. 2014, *ApJ*, **783**, 112
 Beatty, T. G., Morley, C. V., Curtis, J. L., et al. 2018, *AJ*, **156**, 168
 Bento, J., Hartman, J. D., Bakos, G., et al. 2018, *MNRAS*, **477**, 3406
 Bodenheimer, P., Lin, D. N. C., & Mardling, R. A. 2001, *ApJ*, **548**, 466
 Boksenberg, A., Evans, R. G., Fowler, R. G., et al. 1973, *MNRAS*, **163**, 291
 Bonomo, A. S., Sozzetti, A., Santerne, A., et al. 2015, *A&A*, **575**, A85
 Bouchy, F., Deleuil, M., Guillot, T., et al. 2011, *A&A*, **525**, A68
 Bressan, A., Marigo, P., Girardi, L., et al. 2012, *MNRAS*, **427**, 127
 Brown, T. M., Baliber, N., Bianco, F. B., et al. 2013, *PASP*, **125**, 1031
 Buchhave, L. A., Latham, D. W., Carter, J. A., et al. 2011, *ApJS*, **197**, 3
 Buchhave, L. A., Latham, D. W., Johansen, A., et al. 2012, *Natur*, **486**, 375
 Burrows, A., Hubbard, W. B., Lunine, J. I., & Liebert, J. 2001, *RvMP*, **73**, 719
 Carmichael, T. W., Irwin, J. M., Murgas, F., et al. 2022, *MNRAS*, **514**, 4944
 Carmichael, T. W., Quinn, S. N., Zhou, G., et al. 2021, *AJ*, **161**, 97
 Chabrier, G., Johansen, A., Janson, M., & Rafikov, R. 2014, in *Protostars and Planets VI*, ed. H. Beuther et al. (Tucson, AZ: Univ. Arizona Press), 619
 Choi, J., Dotter, A., Conroy, C., et al. 2016, *ApJ*, **823**, 102
 Ciardi, D. R., Beichman, C. A., Horch, E. P., & Howell, S. B. 2015, *ApJ*, **805**, 16
 Claret, A. 2017, *A&A*, **600**, A30
 Collier Cameron, A., Guenther, E., Smalley, B., et al. 2010, *MNRAS*, **407**, 507
 Collins, K. A., Kielkopf, J. F., Stassun, K. G., & Hessman, F. V. 2017, *AJ*, **153**, 77
 Cooke, B. F., Pollacco, D., Almléaky, Y., et al. 2020, *AJ*, **159**, 255
 Cortés-Zuleta, P., Rojo, P., Wang, S., et al. 2020, *A&A*, **636**, A98
 Cutri, R. M., Skrutskie, M. F., van Dyk, S., et al. 2003, *yCat*, **2246**, 0
 Cutri, R. M., Wright, E. L., T. C., et al. 2012, *yCat*, **2311**, 0
 Dahm, S. E. 2015, *ApJ*, **813**, 108
 D'Angelo, G., Kley, W., & Henning, T. 2003, *ApJ*, **586**, 540
 David, T. J., Hillenbrand, L. A., Gillen, E., et al. 2019, *ApJ*, **872**, 161
 Donati, J.-F., Semel, M., Carter, B. D., Rees, D. E., & Collier Cameron, A. 1997, *MNRAS*, **291**, 658
 Dorval, P., Talens, G. J. J., Otten, G. P. P. L., et al. 2020, *A&A*, **635**, A60
 Dotter, A. 2016, *ApJS*, **222**, 8
 Dotter, A., Chaboyer, B., Jevremović, D., et al. 2008, *ApJS*, **178**, 89
 Eastman, J., Gaudi, B. S., & Agol, E. 2013, *PASP*, **125**, 83
 Eastman, J. D., Rodriguez, J. E., Agol, E., et al. 2019, arXiv:1907.09480
 Esteves, L. J., De Mooij, E. J. W., & Jayawardhana, R. 2015, *ApJ*, **804**, 150
 Fabrycky, D., & Tremaine, S. 2007, *ApJ*, **669**, 1298
 Feiden, G. A., & Chaboyer, B. 2012, *ApJ*, **761**, 30
 Foreman-Mackey, D., Hogg, D. W., Lang, D., & Goodman, J. 2013, *PASP*, **125**, 306
 Gaia Collaboration, Vallenari, & Brown, A. 2022, arXiv:2208.00211
 Gaudi, B. S., Stassun, K. G., Collins, K. A., et al. 2017, *Natur*, **546**, 514
 Giacalone, S., Dressing, C. D., García Muñoz, A., et al. 2022, *ApJL*, **935**, L10
 Gill, S., Ulmer-Moll, S., Wheatley, P. J., et al. 2022, *MNRAS*, **513**, 1785
 Gillen, E., Hillenbrand, L. A., David, T. J., et al. 2017, *ApJ*, **849**, 11
 Gray, D. F. 2005, *The Observation and Analysis of Stellar Photospheres* (Cambridge: Cambridge Univ. Press)
 Grieves, N., Bouchy, F., Lendl, M., et al. 2021, *A&A*, **652**, A127
 Guerrero, N. M., Seager, S., Huang, C. X., et al. 2021, *ApJS*, **254**, 39
 Guillot, T. 2005, *AREPS*, **33**, 493
 Guillot, T. 2010, *A&A*, **520**, A27
 Guillot, T., Abe, L., Agabi, A., et al. 2015, *AN*, **336**, 638
 Guillot, T., & Morel, P. 1995, *A&AS*, **109**, 109
 Hattori, S., Foreman-Mackey, D., Hogg, D. W., et al. 2022, *AJ*, **163**, 284
 Hellier, C., Anderson, D. R., Barkaoui, K., et al. 2019, *MNRAS*, **490**, 1479
 Høijmakers, H. J., Ehrenreich, D., Heng, K., et al. 2018, *Natur*, **560**, 453
 Høg, E., Fabricius, C., Makarov, V. V., et al. 2000, *A&A*, **355**, L27
 Hogg, D. W., Bovy, J., & Lang, D. 2010, arXiv:1008.4686
 Hooton, M. J., Hoyer, S., Kitzmann, D., et al. 2022, *A&A*, **658**, A75
 Howell, S. B., Everett, M. E., Sherry, W., Horch, E., & Ciardi, D. R. 2011, *AJ*, **142**, 19
 Howell, S. B., & Furlan, E. 2022, *FrASS*, **9**, 871163
 Howell, S. B., Scott, N. J., Matson, R. A., et al. 2021, *FrASS*, **8**, 165
 Howell, S. B., Sobeck, C., Haas, M., et al. 2014, *PASP*, **126**, 398
 Jenkins, J. M., Twicken, J. D., McCauliff, S., et al. 2016, *Proc. SPIE*, **9913**, 99133E
 Johnson, M. C., Rodriguez, J. E., Zhou, G., et al. 2018, *AJ*, **155**, 100
 Kipping, D. M. 2013, *MNRAS*, **435**, 2152
 Kounkel, M., & Covey, K. 2019, *AJ*, **158**, 122
 Kozai, Y. 1962, *AJ*, **67**, 591
 Kraft, R. P. 1967, *ApJ*, **150**, 551
 Kurucz, R. L. 1992, in *IAU Symp. 149, The Stellar Populations of Galaxies*, ed. B. Barbuy & A. Renzini (Dordrecht: Kluwer), 225
 Lester, K. V., Matson, R. A., Howell, S. B., et al. 2021, *AJ*, **162**, 75
 Lidov, M. L. 1962, *P&SS*, **9**, 719
 Lightkurve Collaboration, Cardoso, J. V. d. M., Hedges, C., et al. 2018, *Lightkurve: Kepler and TESS time series analysis in Python*, Astrophysics Source Code Library, ascl:1812.013
 Lindegren, L., Bastian, U., Biermann, M., et al. 2021, *A&A*, **649**, A4
 Lindegren, L., Hernández, J., Bombrun, A., et al. 2018, *A&A*, **616**, A2
 Lomb, N. R. 1976, *Ap&SS*, **39**, 447
 Lund, M. B., Rodriguez, J. E., Zhou, G., et al. 2017, *AJ*, **154**, 194
 Mandel, K., & Agol, E. 2002, *ApJL*, **580**, L171
 Mann, A. W., Wood, M. L., Schmidt, S. P., et al. 2022, *AJ*, **163**, 156
 Matson, R. A., Howell, S. B., Horch, E. P., & Everett, M. E. 2018, *AJ*, **156**, 31
 Morton, T. D., Bryson, S. T., Coughlin, J. L., et al. 2016, *ApJ*, **822**, 86
 Moutou, C., Bonomo, A. S., Bruno, G., et al. 2013, *A&A*, **558**, L6
 Newton, E. R., Mann, A. W., Tofflemire, B. M., et al. 2019, *ApJL*, **880**, L17
 Paredes, L. A., Henry, T. J., Quinn, S. N., et al. 2021, *AJ*, **162**, 176
 Parviainen, H., Gandolfi, D., Deleuil, M., et al. 2014, *A&A*, **562**, A140
 Patel, J. A., & Espinoza, N. 2022, *AJ*, **163**, 228
 Paxton, B., Bildsten, L., Dotter, A., et al. 2011, *ApJS*, **192**, 3
 Paxton, B., Cantiello, M., Arras, P., et al. 2013, *ApJS*, **208**, 4
 Paxton, B., Marchant, P., Schwab, J., et al. 2015, *ApJS*, **220**, 15
 Phillips, M. W., Tremblin, P., Baraffe, I., et al. 2020, *A&A*, **637**, A38
 Psaridi, A., Bouchy, F., Lendl, M., et al. 2022, *A&A*, **664**, A94
 Rampalli, R., Agüeros, M. A., Curtis, J. L., et al. 2021, *ApJ*, **921**, 167
 Rasio, F. A., & Ford, E. B. 1996, *Sci*, **274**, 954
 Rebull, L. M., Stauffer, J. R., Bouvier, J., et al. 2016, *AJ*, **152**, 113
 Rice, M., Wang, S., & Laughlin, G. 2022, *ApJL*, **926**, L17
 Ricker, G. R., Winn, J. N., Vanderspek, R., et al. 2015, *JATIS*, **1**, 014003
 Rodriguez, J. E., Quinn, S. N., Vanderburg, A., et al. 2023, *MNRAS*, **521**, 2765
 Saumon, D., & Marley, M. S. 2008, *ApJ*, **689**, 1327
 Schlafly, E. F., & Finkbeiner, D. P. 2011, *ApJ*, **737**, 103
 Schlaflman, K. C. 2010, *ApJ*, **719**, 602
 Schlegel, D. J., Finkbeiner, D. P., & Davis, M. 1998, *ApJ*, **500**, 525
 Scott, N. J., Howell, S. B., Gnilka, C. L., et al. 2021, *FrASS*, **8**, 138
 Sebastian, D., Guenther, E. W., Deleuil, M., et al. 2022, *MNRAS*, **516**, 636
 Shporer, A., O'Rourke, J. G., Knutson, H. A., et al. 2014, *ApJ*, **788**, 92
 Siverd, R. J., Beatty, T. G., Pepper, J., et al. 2012, *ApJ*, **761**, 123
 Smith, J. C., Stumpe, M. C., Van Cleve, J. E., et al. 2012, *PASP*, **124**, 1000
 Spiegel, D. S., Burrows, A., & Milsom, J. A. 2011, *ApJ*, **727**, 57
 Stangret, M., Pallé, E., Casasayas-Barris, N., et al. 2021, *A&A*, **654**, A73
 Stassun, K. G., Collins, K. A., & Gaudi, B. S. 2017, *AJ*, **153**, 136
 Stassun, K. G., Oelkers, R. J., Pepper, J., et al. 2018, *AJ*, **156**, 102
 Stassun, K. G., & Torres, G. 2016, *AJ*, **152**, 180
 Stassun, K. G., & Torres, G. 2018, *ApJ*, **862**, 61
 Stassun, K. G., & Torres, G. 2021, *ApJL*, **907**, L33
 Stevens, D. J., Zhou, G., Johnson, M. C., et al. 2020, *MNRAS*, **499**, 3775
 Stumpe, M. C., Smith, J. C., Catanzarite, J. H., et al. 2014, *PASP*, **126**, 100
 Stumpe, M. C., Smith, J. C., Van Cleve, J. E., et al. 2012, *PASP*, **124**, 985

- Talens, G. J. J., Albrecht, S., Spronck, J. F. P., et al. 2017, *A&A*, **606**, [A73](#)
- Thompson, G. I., Nandy, K., Jamar, C., et al. 1995, VizieR On-line Data Catalog, [II/59B](#)
- Thorngren, D. P., & Fortney, J. J. 2018, *AJ*, **155**, [214](#)
- Tingley, B., Endl, M., Gazzano, J. C., et al. 2011, *A&A*, **528**, [A97](#)
- Tofflemire, B. M., Rizzuto, A. C., Newton, E. R., et al. 2021, *AJ*, **161**, [171](#)
- Tokovinin, A. 2018, *PASP*, **130**, [035002](#)
- Tokovinin, A., Fischer, D. A., Bonati, M., et al. 2013, *PASP*, **125**, [1336](#)
- Torres, G., Andersen, J., & Giménez, A. 2010, *A&ARv*, **18**, [67](#)
- Bakos, G. Á., Torres, G., Pál, A., et al. 2010, *ApJ*, **710**, [1724](#)
- Triaud, A. H. M. J. 2018, in *Handbook of Exoplanets*, ed. H. J. Deeg & J. A. Belmonte (Berlin: Springer), [2](#)
- Vanderburg, A., Huang, C. X., Rodriguez, J. E., et al. 2019, *ApJL*, **881**, [L19](#)
- Vanderburg, A., & Johnson, J. A. 2014, *PASP*, **126**, [948](#)
- von Essen, C., Mallonn, M., Piette, A., et al. 2021, *A&A*, **648**, [A71](#)
- Winn, J. N., Fabrycky, D., Albrecht, S., & Johnson, J. A. 2010, *ApJL*, **718**, [L145](#)
- Wu, Y., & Lithwick, Y. 2011, *ApJ*, **735**, [109](#)
- Yan, F., & Henning, T. 2018, *NatAs*, **2**, [714](#)
- Yee, S. W., Winn, J. N., Hartman, J. D., et al. 2022, *AJ*, **164**, [70](#)
- Zhou, G., Huang, C. X., Bakos, G. Á., et al. 2019, *AJ*, **158**, [141](#)
- Zhou, G., Rodriguez, J. E., Collins, K. A., et al. 2016, *AJ*, **152**, [136](#)
- Zhou, G., Rodriguez, J. E., Vanderburg, A., et al. 2018, *AJ*, **156**, [93](#)
- Zhou, G., Winn, J. N., Newton, E. R., et al. 2020, *ApJL*, **892**, [L21](#)
- Ziegler, C., Tokovinin, A., Briceño, C., et al. 2020, *AJ*, **159**, [19](#)